Transitions from Near-Surface to Interior Redox upon Lithiation in Conversion Electrode Materials

Kai He,[†] Huolin L. Xin,[†] Kejie Zhao,[‡] Xiqian Yu,[§] Dennis Nordlund,[‖] Tsu-Chien Weng,[‖] Jing Li,[†,⊥] Yi Jiang,[#] Christopher A. Cadigan,[∇] Ryan M. Richards,[∇] Marca M. Doeff,[°] Xiao-Qing Yang,[§] Eric A. Stach,[†] Ju Li,*[,‡] Feng Lin,*[,∇,°] and Dong Su*[,†,⊥]

[†]Center for Functional Nanomaterials, Brookhaven National Laboratory, Upton, New York 11973, United States

[‡]Department of Nuclear Science and Engineering and Department of Materials Science and Engineering, Massachusetts Institute of Technology, Cambridge, Massachusetts 02139, United States

[§]Chemistry Department, Brookhaven National Laboratory, Upton, New York 11973, United States

[‖]Stanford Synchrotron Radiation Lightsource, SLAC National Accelerator Laboratory, Menlo Park, California 94025, United States

[⊥]Department of Materials Science and Engineering, Stony Brook University, Stony Brook, New York 11794, United States

[#]Department of Physics, Cornell University, Ithaca, New York 14853, United States

[∇]Department of Chemistry and Geochemistry, Materials Science Program, Colorado School of Mines, Golden, Colorado 80401, United States

[°]Environmental Energy Technologies Division, Lawrence Berkeley National Laboratory, Berkeley, California 94720, United States

S *Supporting Information*

ABSTRACT: Nanoparticle electrodes in lithium-ion batteries have both near-surface and interior contributions to their redox capacity, each with distinct rate capabilities. Using combined electron microscopy, synchrotron X-ray methods and ab initio calculations, we have investigated the lithiation pathways that occur in NiO electrodes. We find that the near-surface electroactive ($Ni^{2+} \rightarrow Ni^0$) sites saturated very quickly, and then encounter unexpected difficulty in propagating the phase transition into the electrode (referred to as a "shrinking-core" mode). However, the interior capacity for $Ni^{2+} \rightarrow Ni^0$ can be accessed efficiently following the nucleation of lithiation "fingers" that propagate into the sample bulk, but only after a certain incubation time. Our microstructural observations of the transition from a slow shrinking-core mode to a faster lithiation finger mode corroborate with synchrotron characterization of large-format batteries and can be rationalized by stress effects on transport at high-rate discharge. The finite incubation time of the lithiation fingers sets the intrinsic limitation for the rate capability (and thus the power) of NiO for electrochemical energy storage devices. The present work unravels the link between the nanoscale reaction pathways and the C-rate-dependent capacity loss and provides guidance for the further design of battery materials that favors high C-rate charging.

Near-Surface (NS) Redox   "Finger" Mode   Interior (I) Redox

KEYWORDS: *Lithium ion battery, nickel oxide, conversion reaction, in situ TEM, incubation, rate capability*
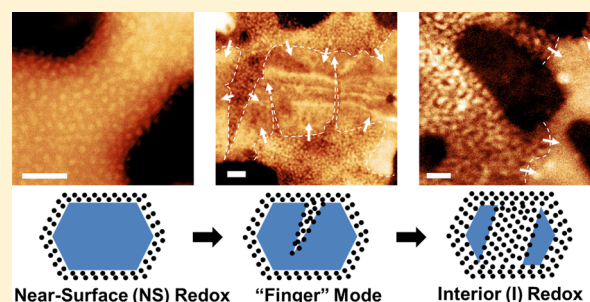
Lithium-ion batteries and supercapacitors both rely on electrochemical redox processes, although different mechanisms determine their relative energy and power densities.[1−5] For nanostructured electrodes of lithium-ion batteries, the capacity contains contributions from redox reactions that occur in both the interior (I) and near-surface (NS) regions.[6−9] It is believed that the interior redox reactions contribute more to the overall battery capacity, but these take a longer time to be activated. In contrast, redox reactions in the near-surface reaction may exhibit a supercapacitor-like behavior (i.e., a high power density) because of the short transport paths for ions and electrons.[7−9] Thus, an understanding of the kinetics of the transition from NS-redox to I-redox is critical to determining the rate capability of a lithium ion battery. Even though the rate

capability and reaction kinetics can be improved by modifications to the material structure (such as surface coating and functionalization) and by architecture engineering,[10−21] it is still not clear how the redox front propagates into the interior, especially at high discharge rates.

In this work, we have integrated complementary atomic resolution transmission electron microscopy (TEM) imaging, electron and X-ray spectroscopies, and electrochemistry measurements to study the kinetics of the lithiation of NiO
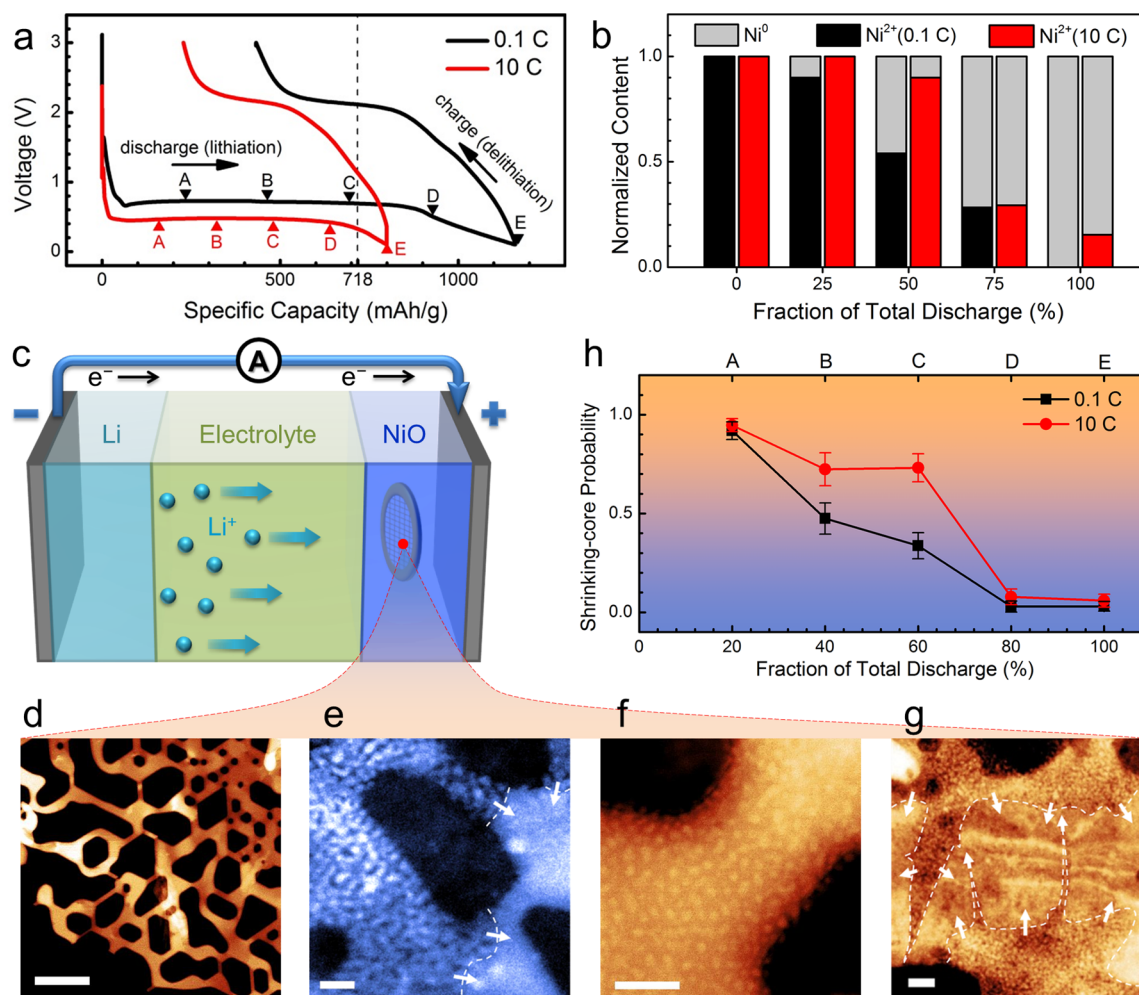
Figure 1. Electrochemical and structural change after lithiation of NiO nanosheets. (a) Charge−discharge curves at rates of 0.1C and 10C. Dashed line indicates the theoretical capacity of 718 mAh/g. (b) Relative content of Ni^{2+} and Ni^0 at different discharge fractions as measured by synchrotron Ni K-edge XAS (original spectra shown in Supporting Information Figure 2). (c) Schematic illustration of an ex situ battery cell with a TEM grid submerged in the active NiO electrode. ADF-STEM images of (d) a pristine NiO nanosheet, (e) an area that has almost been fully lithiated via the bulk mode (Mode B), (f) an area that has been partially lithiated only on surface via the shrinking-core mode (Mode S), and (g) an area that has been partially lithiated via the finger mode (Mode F). Dashed lines and arrows indicate reaction fronts and propagation directions. (h) Probability of surface mode as a function of discharge fraction via 0.1C and 10C discharges. The data points are acquired at the corresponding states labeled A−E in (a). Scale bars, 100 (d), 10 (e,f), and 20 nm (g).

nanosheet electrodes. After visualizing the heterogeneous redox reaction modes at the near-surface and interior regions, we found that the transition from NS-redox to I-redox reaction is exceptionally slow when it occurs through the classic "shrinking-core" mode.[22] Instead, most of the interior $Ni^{2+} \rightarrow Ni^0$ sites are mined only after high-aspect-ratio "reaction fingers" are nucleated. These subsequently penetrate deeply into the nanoparticle interior and then thicken so as to spread the transition through the bulk of the material. There is an "incubation" time, which averages to about 100 s from in situ TEM observations, before the redox reaction can penetrate into the interior. The reaction time scale and patterns we discovered from in situ TEM correlate with the ultimate rate performance of large-format batteries and are further supported by ex situ TEM and X-ray spectroscopies. We believe such heterogeneous transition mechanisms from NS-redox to I-redox may be generic and transferrable to a large class of conversion nanoelectrode materials.

Our experiments were performed using three setups: (I) 2032-type coin cells (Figure 1a,b) using liquid electrolyte, (II) TEM "grid-in-a-coin-cell" using liquid electrolyte for easy postmortem TEM characterization of large-format batteries (Figure 1c−g), and (III) in situ lithiation (Figure 2, 3) using Li_2O solid electrolyte. Setups I, II, and III all use the same NiO nanosheets with holes and faceted surfaces[23,24] as positive electrodes, and Li metal as negative electrodes. For battery performance, the initial formatting cycle is crucial, as the structures inherited from the first cycle may dramatically influence subsequent cycles for conversion electrodes.[25] Therefore, the first cycle, specifically the first lithiation process, as shown in reaction eq 1[26,27] and confirmed by in situ diffraction (Supporting Information Figure S1 and Movie 4), is the focus of the present paper.

$$NiO + 2Li^+ + 2e^-(U) \rightarrow Ni + Li_2O \qquad (1)$$

For setup I, the voltage-total capacity curves are shown in Figure 1a for high (∼10C) and low (∼0.1C) charging rate, respectively. The nominal first-cycle discharge (lithiation) capacities obtained at 10C (800 mAh/g) and 0.1C (1160 mAh/g) are both larger than the theoretical specific capacity
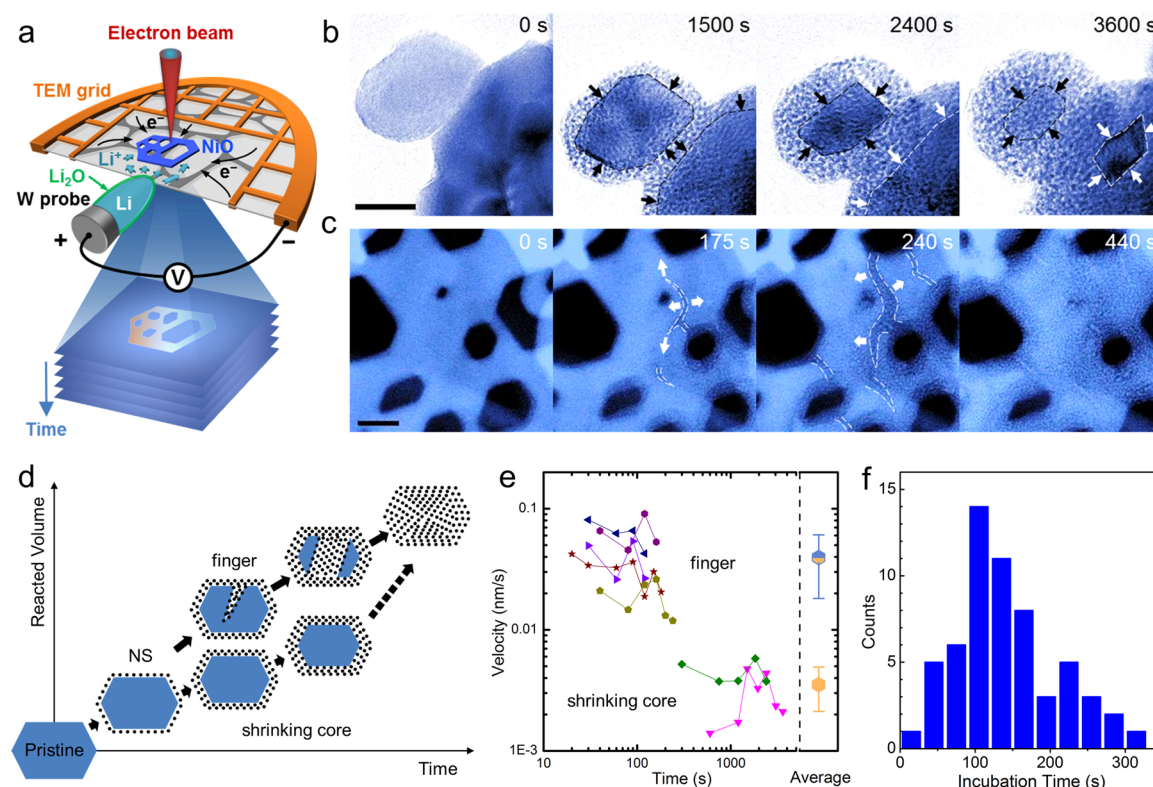
Figure 2. Structural evolution during in situ lithiation of NiO nanosheets. (a) Schematic illustration of in situ electrochemical cell setup. Time-sequenced S/TEM snapshots during in situ lithiation indicate (b) shrinking-core mode, and (c) finger mode. Dashed lines and arrows indicate reaction fronts and propagation directions. (d) Schematic cartoon showing heterogeneous pathways of N → I transitions. (e) The velocity of reaction front propagation in different pathways deduced from numerous time-dependent position measurements (see Supporting Information Figure 6). The modality-correlated velocities exhibit in two groups and their average values are shown in the right panel. (f) Histogram showing statistics of incubation time from numerous finger-mode events. Scale bars, 20 nm.

(718 mAh/g) of NiO. This does not mean full conversion of $Ni^{2+} \rightarrow Ni^0$ centers,[28] however, due to electrolyte decomposition and SEI formation that consume injected electrons: these side reactions become possible for ethylene carbonate/diethyl carbonate liquid electrolyte whenever the voltage U drops below ~1.3 V against Li^+/Li (ref 3). To reveal the actual degree of $Ni^{2+} \rightarrow Ni^0$ conversion in the first discharge, we performed synchrotron hard X-ray absorption spectroscopy[29,30] (XAS, Supporting Information Figure S2) that characterizes the valence state of all Ni atoms contained in a 2032 coin cell. The XAS spectra were fit to a linear combination of Ni^{2+} and Ni^0 spectroscopic components, and the degree of $Ni^{2+} \rightarrow Ni^0$ conversion is indicated in Figure 1b against the fraction of total discharge (FoTD). (Please note that FoTD includes side reactions.) It is interesting to note that at FoTD = 100% all the Ni^{2+} were reduced to Ni^0 in the 0.1C coin cell but in the 10C coin cell ~15% of the Ni^{2+} still remained unreduced. This means that at 10C not all the electroactive sites in NiO nanosheets can be reduced even as the voltage dropped to near zero against Li^+/Li (the equilibrium voltage of eq 1 is 0.6 V against Li^+/Li).[25] This measures the true rate-dependent electrodic capacity of NiO.

It is also interesting to note that very little Ni^{2+} was reduced up to FoTD = 25%, and 0.1C and 10C samples do not differ much in this regard (Figure 1b). This means electrolyte decomposition and SEI formation consume most of electrons injected up to the first quarter of discharge, which is reasonable since SEI formation happens below $U = 1.3$ V[3], earlier than $U_0 = 0.6$ V[25] for reaction 1. For 10C sample, even rather limited

amount of Ni^{2+}/Ni^0 redox happened at the NS region (as observed by TEM), which is difficult to detect due to the low (surface) sensitivity of hard X-ray and the quantification technique using spectral linear combination. But SEI formation kinetics is self-slowing after the SEI thickness has grown. Generally speaking, SEI formation dominates the early part of the first discharge, and 0.1C sample forms more SEI than the 10C sample ($1160-718=442$ mAh/g vs $800-718 \times 0.85=190$ mAh/g, so almost double by the end of the discharge) overall due to the longer reaction time. For the later part of the first discharge, $Ni^{2+} \rightarrow Ni^0$ conversion dominates the total reaction. The difference between 0.1C and 10C samples in this regard is that while the degree of $Ni^{2+} \rightarrow Ni^0$ is almost linear between FoTD = 25−100% at 0.1C, for the 10C sample the $Ni^{2+} \rightarrow Ni^0$ reduction kinetics seems to have a nonlinear behavior. In the 10C sample, there is a small amount of conversion from FoTD = 25−50%, followed by very rapid conversion between FoTD = 50−75% ("inflection"). As 10C means 6 min at full discharge, this inflection stage is quite remarkable in the sense that more than 50% of all the Ni^{2+} in the coin cell is reduced in a time duration $\tau_{inflection}$ ~1.5 min. This indicates that certain intrinsic kinetics in NiO nanosheets[23,24] must be quite fast to be able to accomplish this at nearly a constant voltage ~0.4 V (this driving voltage U barely changed between FoTD = 0−75%). Thus, the "intrinsic" rate capability of NiO nanosheets[23,24] can be quite good.[6] But for the FoTD = 75−100%, for various reasons (e.g., electrolyte decomposition, long-range Li^+/electron transport disruptions, or another possible reason to be suggested later) the previously rapid "inflection" slowed down, even though the
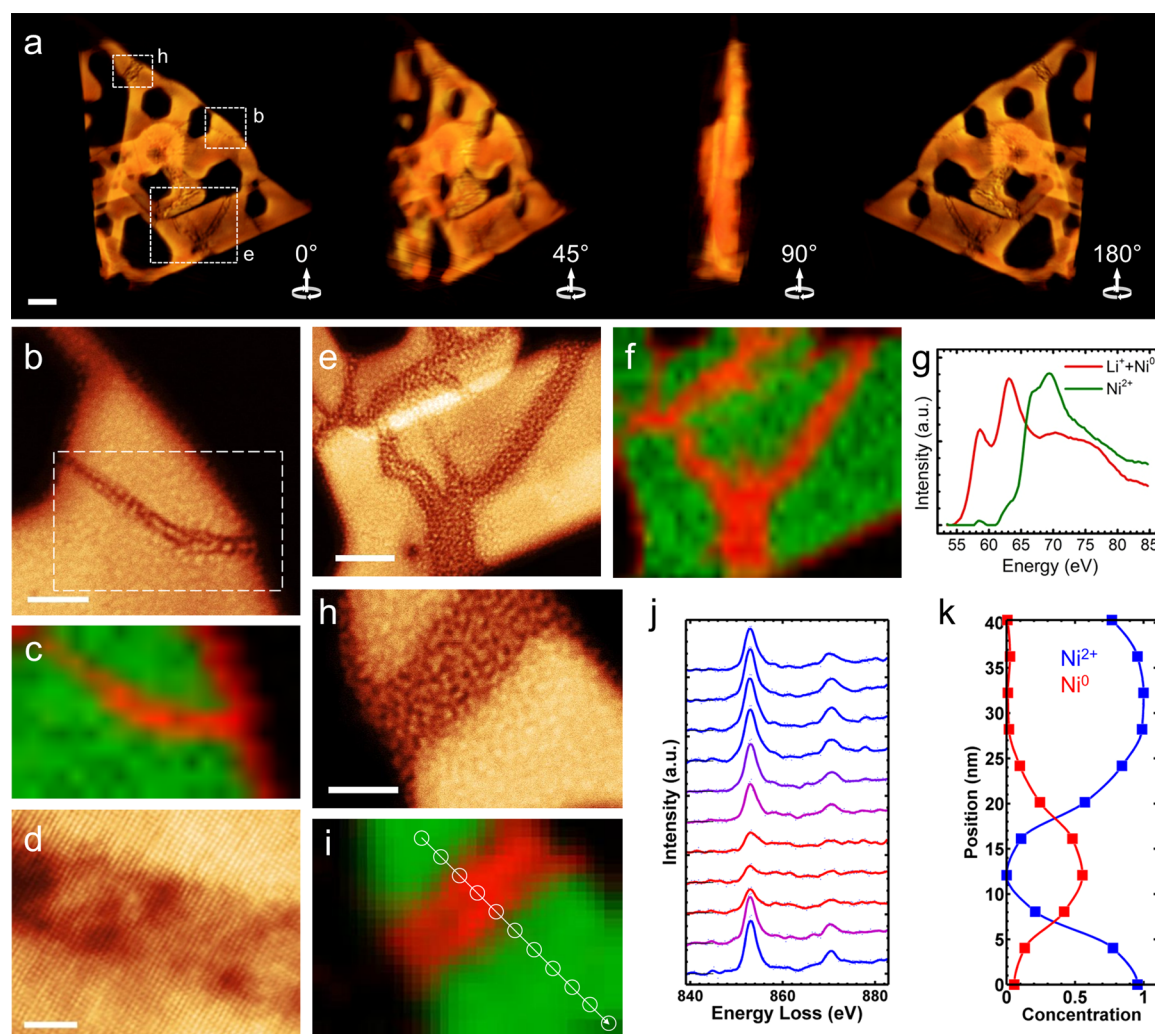
Figure 3. Tomography and EELS mapping of lithiated NiO fingers. (a) A series of reconstructed 3D tomograms from an in situ lithiated NiO nanosheet at viewing angles of 0°, 45°, 90°, and 180°, (also see Supporting Information Movie 5). (b,e,h) Zoom-in ADF-STEM images corresponding to the labeled regions in (a). (c,f) EELS mapping of Ni^{2+} (green) and $Li^{+}+Ni^{0}$ (red) for areas in (b,e) using the low-loss spectra components shown in (g). (d) Atomically resolved STEM image showing a crack region coherently bounded with unlithiated NiO in (b). (i) EELS charge mapping of Ni^{2+} (green) and Ni^{0} (red) for the area in (h), a series of EELS spectra and $Ni^{2+/0}$ concentration profiles along the arrow are shown in (j,k), respectively. Scale bars, 20 (a), 10 (b), 2 (d), 20 (e), and 10 nm (h).

driving voltage U drops more rapidly in the last quarter of discharge and thus increases the reductive driving force. The $Ni^{2+} \rightarrow Ni^{0}$ conversion ended up unfinished, leaving behind 15% unreduced Ni^{2+}. Such nonlinear "incubation–inflection–saturation" coin-cell behavior at time scale of minutes may thus be attributed to an intrinsic NiO electrodic time scale, as opposed to the 0.1C case where the electron supply is throttled externally to be much slower than $\tau_{inflection}$.

We note that a redox time scale of minutes at 10C is on the borderline between what is nominally considered supercapacitor-like behavior and battery behavior ($\tau_{inflection}$ ~1.5 min would be considered fast in the battery context, but slow in the redox supercapacitor context). Conventional understanding of the operation of lithium ion batteries involves consideration of both near-surface electroactive sites and interior electroactive sites. However, there are few direct characterizations of either the NS or I behaviors and observations of the NS → I transition are few. In order to understand how discharge rate actually drives changes in the material's microstructure, we have utilized the TEM "grid-in-a-coin cell" method[23] as illustrated in Figure

1c (setup II). This approach allows us to subject NiO to states of charge that mimic the situation in a fully operational battery, yet are directly amenable to TEM imaging. The pristine NiO materials are ~20 nm thick sheets with closely packed {111} basal planes forming the largest free surfaces, and they are initially perforated with hexagonal holes that are bounded by {112} facets enabling short diffusion paths from NS to I redox sites (Figure 1d and Supporting Information Figure S3).[23,24] The uniform and thin thickness is natively electron-transparent and thus suitable for in situ TEM observations, particularly for large-scale in-plane lithiation propagation. The discharged samples usually contained a significant fraction of unreacted NiO (unreduced Ni^{2+}), with the reacted regions consisting of fine metallic Ni nanoparticles (Supporting Information Figure S4) embedded in a Li_2O matrix or covering the NiO surface (Figure 1e–g). Critically, for both C-rates we found three distinct, heterogeneous morphologies that differed in their relative amounts. The three lithiation modes are called Modes bulk (B), shrinking-core (S), and finger-like (F) and their appearance is described in detail below.

In Mode B (bulk mode), the reaction front has advanced deeply inside the NiO interior (Figure 1e) with the reaction front normal $\mathbf{n} \perp [111]$. The reaction front is relatively flat, exhibits no strong crystallographic preference in its propagation direction (except for $\perp [111]$), and is sharply bounded by unreacted NiO. In Mode S (shrinking-core mode), the reaction appears to have first proceeded very rapidly along all surfaces by surface diffusion (later verified by in situ observations) and then thickens further uniformly perpendicular to all surfaces, including the (111) surfaces[22] (Figure 1f). Mode F (finger mode) exhibits a strikingly different morphology: a high-aspect-ratio lithiation finger $\perp [111]$ penetrates deep inside the unreacted material. Mode F has an overall appearance similar to that of a crack or wedge, although its microscopic manifestation is the reaction of NiO to Ni + Li_2O and not the cleavage of a material as would be observed in a crack (Figure 1g). In order to understand the correlation between the reaction morphology and the discharge rates, we imaged a large number of nanosheets reacted ex situ to a specified FoTD (20, 40, 60, 80, and 100%, corresponding to the points labeled A, B, C, D, and E in Figure 1a, respectively) at both 10C and 0.1C. Figure 1h summarizes the statistics obtained from the TEM images, which were collected in an unbiased manner (see an example in Supporting Information Figure S5). We see a distinct difference in the prevalence of different reaction morphologies as a function of the discharge rate: the high C-rate samples show a higher prevalence of Mode S (shrinking-core mode), while the low C-rate favors Mode B (bulk mode). Moreover, as the particle-ensemble FoTD advances, the 10C reaction morphology switched from being primarily Mode S to Mode B.

While a rigorous statistical link is established between the rate and the reaction modes at particles-ensemble level in Setup II, ex post facto imaging of this type cannot provide time-dependent trajectory of the NS → I reaction transition. In order to investigate this phenomenon further, we have utilized a real-time electron microscopy approach (Setup III) to investigate the reaction kinetics for the different modes. The in situ experiments utilized a dry electrochemical cell with no side reaction of organic electrolyte decomposition.[31−33] As illustrated in Figure 2a, Li ions are transferred toward the NiO electrode under a positive bias in a potentiostatic mode. In the in situ discharging experiments (Supporting Information Movies 1−2), even though there is no deliberate control of the discharge rates, we repeatedly and reproducibly observed the same reaction modes as in the ex situ cells (Figure 2b,c); this indicates that this in situ method is able to provide valid information that can be correlated with the ex post facto observations. In Figure 2b as well as Supporting Information Movie 1, we observed that the surface wetting is very fast by surface diffusion and the redox front propagates from the outer surface (after NS sites have been saturated). Such further propagation (via the shrinking core mode) encounters unexpected difficulty when trying to access the interior and proceeds rather slowly perpendicular to all surfaces of the nanosheet, including (111) surfaces.

However, we also found other pathways for the NS → I transition through the nucleation and subsequent growth of lithiation fingers, which occurred heterogeneously throughout the sheet (Figure 2c). The fingers initially nucleate on ⟨112⟩ facets randomly, a while after the near-surface sites saturate, then elongate $\perp [111]$ until the exits on the opposite surface of the NiO nanosheet. After penetrating all the way through, they then thicken into the nanosheet bulk. At the fully discharged

state, the fingers have thickened enough to completely merge and therefore few identifiable fingers can be seen at FoTD = 100%. From the in situ observations, we found that Mode B occurred after the fingers in Mode F have thickened significantly and/or merged. We thus propose that Mode B occurs after the fingers have formed and thus facilitated Li^+/e^- supply through the interior. After the formation of fingers, the long-range transport capability through interior of the NiO nanosheets is improved and thus promotes the transition to Mode B. At no time were the nanosheets broken. This is in contrast to observations of true material fracture observed in Si nanoparticle[34,35] and ZnO nanowire[36] anode materials.

The complete picture of the reaction pathways for NiO nanosheets is depicted in Figure 2d, where two types of transitions from NS → I are observed: the shrinking-core mode and the finger mode, whereas the I → I transition is proceeded through bulk mode (Mode B, Supporting Information Movie 3). The fact that more Mode B events are observed in low-rate discharged sample implies that after more finger penetrations have been established the lithiation process is promoted. Using Supporting Information Movies 1 and 2, a quantitative analysis of the front propagation speed reveals a large difference between the shrinking-core and the finger modes, as shown in Figure 2e and Supporting Information Figure S6. After the finger has nucleated, the finger mode propagates at average speed of 0.045 nm/s, which is an order of magnitude faster than the shrinking-core mode. Therefore, we can deduce that the NS → I transition is more likely to happen via the finger mode than the shrinking-core mode, after the surfaces have reached a point where the near-surface sites are fully saturated. There appears to be an energy barrier against NS → I transition, which is lower for the more heterogeneous finger mode than for the shrinking-core mode. Before the finger nucleates, there appears to be an incubation time; we saw that the fingers generally do not form immediately after saturation of the near surface sites. We have collected the statistics of finger nucleation, shown in Figure 2f, and found that the characteristic incubation time $\tau_{incubation}$, defined as the average time lapse for the first finger to appear after near-surface site saturation in an area containing 1 hole on average (taken to be the characteristic in-plane length scale of the NiO nanosheet, around 30 nm), is ∼100 s. During the incubation, Li ions were transported to an interior redox site at near-surface and accumulated until nucleating a lithiation finger. This single-particle time scale matches reasonably well with the aforementioned coin-cell intrinsic time scale $\tau_{incubation}$ ∼ 1.5 min (FoTD = 0−25%) for Setup I. Therefore, a possible interpretation of the XAS results in Figure 1b is that in our coin-cell particle ensemble, after the surface/interfacial transport channels are activated and saturated, it takes time for the fingers to nucleate, elongate, and thicken to access the interior capacity. At 0.1C (36 000 s for a full discharge), there is plenty of time for fingers to nucleate, so the microstructural evolution is throttled externally by electron supply. But at 10C (360 s discharge) a significant fraction of the characteristic in-plane areas will not be able to incubate even one finger due to the intrinsic time scale limitation of $\tau_{incubation}$, and therefore some Ni^{2+} can remain unreduced at FoTD = 100% even as the voltage is drastically lowered. With this assumption, the natural demarcation on the time axis to separate supercapacitor-like behavior from battery-like behavior would be $\tau_{discharge}$ ∼ 100 s, or around 30C. This means that the interior capacity can only be substantially utilized for galvanostatic rates slower than 30C; otherwise only the near-surface capacity can be utilized. A
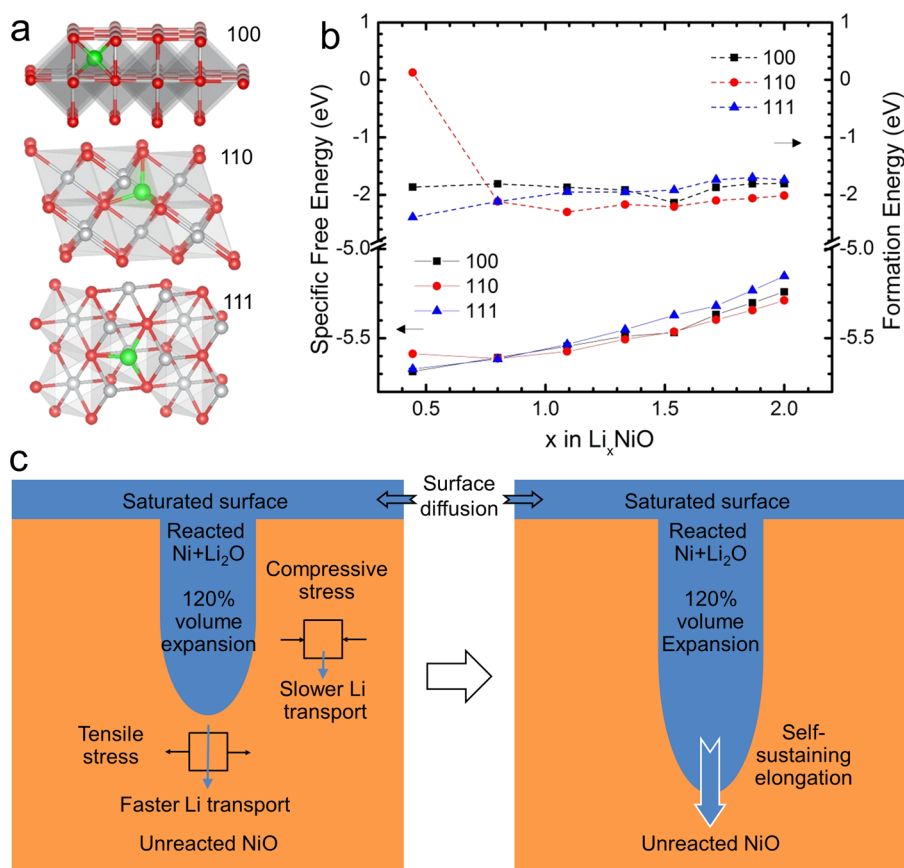
Figure 4. First-principles calculations and stress-induced growth. (a) The geometric feature of crystalline NiO for a lithium atom transport along the ⟨100⟩, ⟨110⟩, and ⟨111⟩ directions (Ni-gray, O-red, Li-green). (b) Formation energy and specific free energy as a function of lithium content when NiO is lithiated along the ⟨100⟩, ⟨110⟩, and ⟨111⟩ orientations. (c) Illustration of stress-induced self-sustaining finger growth.

verifiable prediction from our theory is therefore that if the galvanostatic rate is higher than 30C, our NiO nanosheets can only be used in the "supercapacitor" fashion, meaning that they exhibit a much reduced capacity (viewed in the battery context), even if the long-range transport limitation associated with Li ion in organic electrolyte were to be removed.[37] The intrinsic kinetic time scale extracted from our in situ TEM, $\tau_{incubation}$, does seem to match both our own coin-cell data as well as the general understanding of how NiO should perform at high rates.[37]

In order to understand the finger nucleation and propagation processes in more detail, we utilized analytical scanning transmission electron microscopy (STEM) to study the Mode F regions immediately following their formation. Reconstructed three-dimensional (3D) STEM electron tomograms clearly show that the Mode F reaction fronts form deep 3D penetrations into the NiO slab (Figure 3a and Supporting Information Movie 5). High-magnification STEM images (Figure 3b,e,h) indicate that fingers nucleate and grow into the sample bulk only after the local surfaces have fully saturated. We further explored the reaction chemistry at the nanoscale through electron energy-loss spectroscopic (EELS) mapping (Figure 3c,f,i). These maps indicate that both metallic Ni^0 and Li^+ are present at the sample surface and within the penetration grooves (finger regions). In addition, we have captured an early phase finger groove at atomic resolution as shown in Figure 3d.

From both ex situ and in situ TEM experiments, we observed that the lithiation of NiO disfavors propagation along ⟨111⟩. To interpret this, using ab initio calculations based on density functional theory, we calculated the formation energies and the migration energies along the ⟨100⟩, ⟨110⟩, and ⟨111⟩ directions at various Li concentrations (Figure 4a,b). We found that Li^+ transport along ⟨100⟩ and ⟨110⟩ directions is preferred. From the structural view shown in Figure 4a, it is thus plausible that Li ions transport more readily along in-plane orientations (⟨100⟩ and ⟨110⟩) where open channels are available for Li-ion insertion, whereas the diffusion pathway along the ⟨111⟩ orientation is blocked by front neighbor atoms.

Given that full lithiation can generate a volumetric strain up to 120% (Supporting Information Figure S7), the finger mode may be interpreted as a spontaneous symmetry-breaking instability (Figure 4c) in which the effect of self-stress on Li-ion diffusion plays a key role in perpetuating the long-aspect ratio growth, until the lithiation finger reaches the opposite surface, at which point it has to thicken. In contrast, the slow kinetics of the shrinking-core mode can be understood from a finite deformation model (Supporting Information Figure S8 and S9). In the circumferential (or core−shell) mode, the material is under three-dimensional constraints, which induces a triaxial stress field. This regulates the reaction in a more significant manner. This is consistent with recent studies that showed that a sufficiently large pressure at the interface of crystalline silicon could stop the lithiation reaction.[38] Stress, which is closely related to grain boundaries and other structural defects, may also affect short-range electron transfer[39] and phase boundary mobility,[40] and stress-relief induced contact network disruptions can alter the long-range transport routes of electrons and ions. Thus, the overall evolution can be quite

complicated in an actual battery where conductive carbon black, binder, and the size and morphology of active material particles and the presence of the SEI all could play significant roles. Nonetheless, we believe the intrinsic electrodic time scale limitation measured by both our in situ, and post-mortem method, $\tau_{\text{incubation}}$ ~100 s and $\tau_{\text{inflection}}$ ~1.5 min, has an important bearing on both "high-rate" batteries as well as potentially on "low-rate" redox supercapacitors. We also identified that local stresses can be used to improve reaction kinetics, which can be leveraged as a new design rule for electrode materials engineering for high C-rate lithium ion battery systems. Our findings of surface-to-bulk phenomenon and rate-dependent lithiation mechanisms in NiO system could be generically applicable to conversion electrode materials, though optimization of morphologies, facets, and sizes may be further helpful to improve redox kinetics.

Methods. *Sample Preparation.* The active material (NiO nanosheets) was synthesized using a solvothermal method aided with an alcohol pseudosupercritical drying technique.[24] $Ni(NO_3)_2 \cdot 6H_2O$, urea, and benzyl alcohol were added into 50 mL of methanol with a molar ratio of 2:1:4. The solution was stirred for 1 h and transferred to an autoclave (Parr Reactor, model 4520). The reaction mixture was purged with Ar for 1 min and then Ar was filled with a pressure of 9 bar before initiating the heating process. The mixture was heated to 265 °C and maintained for 1.5 h. Finally, the vapor inside was vented (i.e., pseudosupercritical drying process). A green powder was collected and subsequently calcined at 500 °C for 6 h to yield NiO nanosheets.

Electrochemical Measurements. Composite electrodes were prepared with 80 wt % active material, 10 wt % polyvinylidene fluoride (PVDF), and 10 wt % acetylene carbon black in *N*-methyl-2-pyrrolidone (NMP) and cast onto copper current collectors. The 2032-type coin cells were assembled in an argon-filled glovebox using the composite electrode as the positive electrode and Li metal as the negative electrode. A Celgard separator 2400 and 1 M $LiPF_6$ electrolyte solution in 1:1 w/w ethylene carbonate/diethyl carbonate were used to fabricate coin cells. Battery testing was performed on a computer controlled VMP3 channels (BioLogic). 1C was defined as full discharging NiO in 1 h, which corresponds to a theoretical specific current density of 718 mA/g.

Synchrotron XAS. Ni K-edge XAS measurements were carried out at beamline X18A (NSLS, BNL) in transmission mode using a Si (111) double-crystal monochromator detuned to the 35% value of its original maximum intensity to eliminate the high order harmonics.[28] X-ray absorption near edge structure data was analyzed by ATHENA software package. The linear combination fitting by using the spectra of two end members (NiO and Ni) as the standards achieved the accurate Li stoichiometry in Li_xNiO_2 at each reaction stage, illustrated by Figure 1b.

TEM Characterization. The in situ TEM electrochemical cell was incorporated into a Nanofactory TEM-STM specimen holder (Figure 2a) in which NiO nanosheets dispersed onto a TEM half-grid with amorphous carbon support are analogous to the NiO-C composite electrode, Li metal is coated onto a piezo-driven W probe as the counter electrode with a thin layer of Li_2O formed on Li metal as the solid electrolyte. The Li and NiO were loaded onto the holder in an Ar-filled glovebox and then transferred to TEM column using a sealed Ar bag to avoid air exposure. During the in situ electrochemical tests, a constant negative dc potential was applied to NiO electrode against the Li source during the lithiation process, and the lithiation processes were captured by real-time imaging in either TEM or STEM mode. Electron tomography of the in situ lithiated sample was acquired in ADF-STEM mode with tilt series from −70° to 70° and 1° intervals. The ex situ samples after discharge in coin cells were examined at a large number of lithiated locations to reveal statistical probability of surface or bulk reaction modalities. The total area we checked for each sample was about a few hundreds of micrometers by a few hundreds of micrometers. The in situ measurements and tomography were performed on a JEOL 2100F TEM operated at 200 kV. The high-resolution imaging and analytical EELS were conducted on a Hitachi HD2700C STEM operated at 200 kV and equipped with a probe aberration corrector (spatial resolution <1 Å, energy resolution 0.35 eV). The 3D tomography was reconstructed using the e⁻Tomo software suite written by Robert Hovden et al. (Cornell Muller group) and visualized by Avizo 6.3.

Theoretical Calculations. The first-principles calculations based on density functional theory were performed using Vienna ab initio simulation package (VASP). The projector-augmented wave pseudopotentials were employed and the general gradient approximation for the exchange-correlation functional was used. We construct the crystalline NiO models of [100]-[010]-[001] and [$\bar{1}$10]- [111]- [11$\bar{2}$] orientations, which contain 96 atoms with periodic boundary conditions. The atomic structures and system energy are calculated with an energy cutoff of 400 eV. In energy optimization calculations, the atomic coordinates, the supercell shape, and volume were relaxed. The energy optimization was considered complete when the magnitude of the force on each atom was smaller than 0.04 eV Å^{-1}.

Finite element analysis and simulations based on continuum theory of finite deformation were performed both analytically and numerically using COMSOL Multiphysics software suites; for details see Supporting Information.

■ ASSOCIATED CONTENT

ⓈSupporting Information

Additional details of S/TEM, XAS, DFT calculation, and in situ movies. This material is available free of charge via the Internet at http://pubs.acs.org.

■ AUTHOR INFORMATION

Corresponding Authors
*E-mail: (J.L.) liju@mit.edu.
*E-mail: (F.L.) flin@lbl.gov.
*E-mail: (D.S.) dsu@bnl.gov.

Author Contributions

◼ REFERENCES

(1) Tarascon, J. M.; Armand, M. *Nature* **2001**, *414*, 359−367.

(2) Whittingham, M. S. *Chem. Rev.* **2004**, *104*, 4271−4301.

(3) Goodenough, J. B.; Kim, Y. *Chem. Mater.* **2010**, *22*, 587−603.

(4) Arico, A. S.; Bruce, P.; Scrosati, B.; Tarascon, J. M.; Van Schalkwijk, W. *Nat. Mater.* **2005**, *4*, 366−377.

(5) Simon, P.; Gogotsi, Y.; Dunn, B. *Science* **2014**, *343*, 1210−1211.

(6) Kang, B.; Ceder, G. *Nature* **2009**, *458*, 190−193.

(7) Conway, B. E. *J. Electrochem. Soc.* **1991**, *138*, 1539−1548.

(8) Simon, P.; Gogotsi, Y. *Nat. Mater.* **2008**, *7*, 845−854.

(9) Wang, G.; Zhang, L.; Zhang, J. *Chem. Soc. Rev.* **2012**, *41*, 797−828.

(10) Kang, K.; Meng, Y. S.; Breger, J.; Grey, C. P.; Ceder, G. *Science* **2006**, *311*, 977−980.

(11) Doeff, M. M.; Hu, Y.; McLarnon, F.; Kostecki, R. *Electrochem. Solid-State Lett.* **2003**, *6*, A207−A209.

(12) Liu, H.; Strobridge, F. C.; Borkiewicz, O. J.; Wiaderek, K. M.; Chapman, K. W.; Chupas, P. J.; Grey, C. P. *Science* **2014**, *344*, 1252817.

(13) Xu, B.; Fell, C. R.; Chi, M.; Meng, Y. S. *Energy Environ. Sci.* **2011**, *4*, 2223−2233.

(14) Fong, R.; von Sacken, U.; Dahn, J. R. *J. Electrochem. Soc.* **1990**, *137*, 2009−2013.

(15) Poizot, P.; Laruelle, S.; Grugeon, S.; Dupont, L.; Tarascon, J. M. *Nature* **2000**, *407*, 496−499.

(16) Hu, Y. S.; Guo, Y. G.; Sigle, W.; Hore, S.; Balaya, P.; Maier, J. *Nat. Mater.* **2006**, *5*, 713−717.

(17) Bruce, P. G.; Scrosati, B.; Tarascon, J. M. *Angew. Chem., Int. Ed.* **2008**, *47*, 2930−2946.

(18) Lee, K. T.; Cho, J. *Nano Today* **2011**, *6*, 28−41.

(19) Chan, C. K.; Peng, H.; Liu, G.; McIlwrath, K.; Zhang, X. F.; Huggins, R. A.; Cui, Y. *Nat. Nanotechnol.* **2008**, *3*, 31−35.

(20) Liu, N.; Lu, Z.; Zhao, J.; McDowell, M. T.; Lee, H. W.; Zhao, W.; Cui, Y. *Nat. Nanotechnol.* **2014**, *9*, 187−192.

(21) Zheng, G.; Lee, S. W.; Liang, Z.; Lee, H. W.; Yan, K.; Yao, H.; Wang, H.; Li, W.; Chu, S.; Cui, Y. *Nat. Nanotechnol.* **2014**, *9*, 618−623.

(22) Srinivasan, V.; Newman, J. *J. Electrochem. Soc.* **2004**, *151*, A1517−A1529.

(23) Lin, F.; Nordlund, D.; Weng, T. C.; Zhu, Y.; Ban, C.; Richards, R. M.; Xin, H. L. *Nat. Commun.* **2014**, *5*, 3358.

(24) Hu, J.; Zhu, K.; Chen, L.; Yang, H.; Li, Z.; Suchopar, A.; Richards, R. *Adv. Mater.* **2008**, *20*, 267−271.

(25) Cabana, J.; Monconduit, L.; Larcher, D.; Palacin, M. R. *Adv. Mater.* **2010**, *22*, E170−E192.

(26) Varghese, B.; Reddy, M. V.; Zhu, Y.; Lit, C. S.; Hoong, T. C.; Rao, G. V. S.; Chowdari, B. V. R.; Wee, A. Y. S.; Lim, C. T.; Sow, C. H. *Chem. Mater.* **2008**, *20*, 3360−3367.

(27) Zhou, G.; Wang, D. W.; Yin, L. C.; Li, N.; Li, F.; Cheng, H. M. *ACS Nano* **2012**, *6*, 3214−3223.

(28) Hu, Y. Y.; Liu, Z.; Nam, K. W.; Borkiewicz, O. J.; Cheng, J.; Hua, X.; Dunstan, M. T.; Yu, X.; Wiaderek, K. M.; Du, L. S.; Chapman, K. W.; Chupas, P. J.; Yang, X. Q.; Grey, C. P. *Nat. Mater.* **2013**, *12*, 1130−1136.

(29) Yu, X.; Lyu, Y.; Gu, L.; Wu, H.; Bak, S. M.; Zhou, Y.; Amine, K.; Ehrlich, S. N.; Li, H.; Nam, K. W.; Yang, X. Q. *Adv. Energy Mater.* **2014**, *4*, 1300950.

(30) Chueh, W. C.; Gabaly, F. E.; Sugar, J. D.; Bartelt, N. C.; McDaniel, A. H.; Fenton, K. R.; Zavadil, K. R.; Tyliszczak, T.; Lai, W.; McCarty, K. F. *Nano Lett.* **2013**, *13*, 866−872.

(31) He, K.; Zhou, Y.; Gao, P.; Wang, L.; Pereira, N.; Amatucci, G. G.; Nam, K. W.; Yang, X. Q.; Zhu, Y.; Wang, F.; Su, D. *ACS Nano* **2014**, *8*, 7251−7259.

(32) Liu, X. H.; Wang, J. W.; Huang, S.; Fan, F.; Huang, X.; Liu, Y.; Krylyuk, S.; Yoo, J.; Dayeh, S. A.; Davydov, A. V.; Mao, S. X.; Picraux, S. T.; Zhang, S.; Li, J.; Zhu, T.; Huang, J. Y. *Nat. Nanotechnol.* **2012**, *7*, 749−756.

(33) Gu, M.; Kushima, A.; Shao, Y.; Zhang, J. G.; Liu, J.; Browning, N. D.; Li, J.; Wang, C. *Nano Lett.* **2013**, *13*, 5203−5211.

(34) McDowell, M. T.; Ryu, I.; Lee, S. W.; Wang, C.; Nix, W. D.; Cui, Y. *Adv. Mater.* **2012**, *24*, 6034−6041.

(35) Liu, X. H.; Liu, Y.; Kushima, A.; Zhang, S.; Zhu, T.; Li, J.; Huang, J. Y. *Adv. Energy Mater.* **2012**, *2*, 722−741.

(36) Kushima, A.; Liu, X. H.; Zhu, G.; Wang, Z. L.; Huang, J. Y.; Li, J. *Nano Lett.* **2011**, *11*, 4535−4541.

(37) Feng, L.; Zhu, Y.; Ding, H.; Ni, C. *J. Power Sources* **2014**, *267*, 430−444.

(38) Zhao, K.; Pharr, M.; Wan, Q.; Wang, W. L.; Kaxiras, E.; Vlassak, J. J.; Suo, Z. *J. Electrochem. Soc.* **2012**, *159*, A238−A243.

(39) Bai, P.; Bazant, M. Z. *Nat. Commun.* **2014**, *5*, 3585.

(40) Yang, H.; Huang, S.; Huang, X.; Fan, F.; Liang, W.; Liu, X. H.; Chen, Q. L.; Huang, J. Y.; Li, J.; Zhu, T.; Zhang, S. *Nano Lett.* **2012**, *12*, 1953−1958.